Strain-Rate Sensitivity, Tension-Compression Asymmetry, *r*-Ratio, Twinning, and Texture Evolution of a Rolled Magnesium Alloy Mg-1.3Zn-0.4Ca-0.4Mn

EVGENII VASILEV, NICHOLAS C. FERRERI, RAY DECKER, IRENE J. BEYERLEIN, and MARKO KNEZEVIC

In this work, the deformation response, texture evolution, and twinning development of a magnesium (Mg) alloy, Mg-1.3Zn-0.4Ca-0.4Mn, for biocompatible applications are investigated. Further, the alloy's formability, by examining the instantaneous *r*-ratio and strain-rate sensitivity (SRS) as a function of strain and loading direction, is investigated. It is found that after rolling and peak aging, the alloy has a rolled texture of moderate intensity with the basal planes contained in the rolling plane and with a bimodal, fine-grained microstructure. The alloy shows both high room-temperature tensile strength (300 MPa) and ductility (25 pct) in the rolling direction (RD) and, remarkably, *r*-ratios saturating close to unity in all three in-plane testing directions. It is also found that the SRS is relatively high and uniform, with averages ranging from 0.015 to 0.025, depending on the in-plane testing directions. These are outstanding properties compared to pure Mg and most of its biocompatible alloys. Typical of Mg alloys, this alloy has a propensity for twinning by multiple twin modes, which leads to rapid texture evolution, anisotropy, and tension-compression (T-C) asymmetry in yield stress, with compression having the weaker response. These mechanical characteristics along with their microstructural origins are presented and discussed in this article.

https://doi.org/10.1007/s11661-020-05841-x

I. INTRODUCTION

IN the surgical practice of fracture treatment, temporary implants made of titanium alloys or stainless steel are widely used. Although of sufficient mechanical strength, these materials can adversely affect bone tissue integrity as well as introduce toxic elements. Recently, with well-selected alloying elements, many magnesium (Mg) alloys have been considered as viable candidates for biomedical applications due to a balance of good mechanical properties, light weight, and biocompatibility. Mg is a unique material for *in-vivo* use since it can be gradually resorbed and, at the same time, provide desirable mechanical support throughout the entire period of recovery.[1,2] After their development, many studies on the use of these Mg alloys in the biomedical field initiated in the 1990s.[3–5]

To date, biomedical Mg alloys are used as screws, pins, and bone implants and, therefore, must have a sufficient level of mechanical properties.[6] High-purity Mg, although it has a good biocompatibility, has poor mechanical properties, which hinders its use in many practical applications. Alloying Mg becomes an important method for enhancing the mechanical properties. The choice of alloying elements, however, is crucial as they affect not only mechanical properties, but also corrosion resistance and, as mentioned, overall human health.

Because they are biodegradable and moderately resistant to corrosion, Mg-Zn-Ca-based alloys, as well as those further microalloyed with Zr, Mn, or other nontoxic elements, have received great interest as low-cost structural biocompatible materials.[7–16] With grain-boundary strengthening,[17,18] solid solution hardening,[14] and precipitation hardening,[9,19,20] they can be made with relatively high strengths. In this work, we study a new biomedically relevant Mg alloy, BIOMG 250,*[21,22] in which calcium (Ca), zinc (Zn), and manganese (Mn) are alloying elements. The alloy design used both larger and smaller atoms than

EVGENII VASILEV, NICHOLAS C. FERRERI, and MARKO KNEZEVIC are with the Department of Mechanical Engineering, University of New Hampshire, Durham, NH 03824. Contact email: marko.knezevic@unh.edu RAY DECKER is with nanoMAG LLC, 13753 Otterson Ct, Livonia, MI 48150. IRENE J. BEYERLEIN is with the Mechanical Engineering Department, Materials Department, University of California, Santa Barbara, CA 93106.

Manuscript submitted December 21, 2019.
Article published online June 14, 2020

*BIOMG 250 is a trademark of nanoMag, LLC, Livonia, MI.

the Mg atom to promote cosegregation of alloying elements in the Mg matrix. Alloying with Zn, Ca, and Mn improves the strength of Mg alloys and, thus, provides the necessary support for damaged tissue/bone[7,21,23]; at the same time, these elements are nontoxic to the human body.[21] Mn, along with Ca and Zn, can increase formability according to the density function theory calculations,[24] by modifying pyramidal slip—thus substituting to attain the "rare earth" (RE) effect.

Zn is one of the most common nutritional components and a cofactor for specific enzymes in bone tissue. It is also an effective additive for improving the mechanical properties of Mg alloys.[25] In particular, Zn promotes both solid solution strengthening and precipitation hardening.[11,14,26] However, while Zn has a high solubility limit (6.2 wt pct) in Mg, a recent study reported that excessive Zn additions can promote corrosion rates, due to the formation of Zn-rich intermetallic particles that act as cathodic sites.[10,27]

Ca is an essential element in the human body and the main component in human bone.[28] Ca has been found to weaken the basal texture, characteristic of rolled Mg-based alloy, and thus improve uniformity in properties.[18] However, more than 1 wt pct Ca can deteriorate the corrosion resistance of Mg-Zn-Ca-based alloys.[29] The effect of Ca on mechanical properties is ambiguous. Although the yield strength increases from about 30 to 35 MPa for pure Mg to about 95 MPa for Mg-0.9Ca, the relative elongation decreases from 10 to 12 pct to 2 to 3 pct, respectively, which makes ternary or greater component systems more promising compared to binary systems. In addition, Ca forms Mg_2Ca intermetallics that improve creep strength.[9,30]

Mn can reduce grain size and increase the tensile strength of Mg alloys,[31] as well as increase ductility.[32] Additionally, in small amounts, further additions of Mn have been shown to improve the strength of these Mg-Zn-Ca-based alloys by the grain-boundary strengthening effect.[10,12,33] One of the most important functions of Mn in Mg alloys is to improve the corrosion resistance by converting metals (*e.g.*, iron) that can initiate corrosion into relatively harmless intermetallic compounds such as $Al_6Mn(Fe)$ and $Al_3Mn(Fe)$. Mn is an essential element for playing an important role in metabolic cycles and activation of numerous enzyme systems.[34,35] However, a high concentration of Mn can cause toxicological damage to the nervous system.[36]

In addition to strength, one concern with Mg alloys is formability, the ability to shape the material without cracking. Due to the low symmetry of its hexagonal lattice, Mg and its alloys have a limited number of easy slip systems, which leads to low ductility at room temperature and the need to activate alternative mechanisms such as deformation twinning.[37–43] At room temperature, basal slip in favorably oriented grains can be easily activated. Other slip systems (prismatic and pyramidal) are also activated, especially at elevated temperatures.

The formability of a material is conventionally determined by developing a forming limit diagram (FLD) for the material. Building a FLD, however, requires a broad suite of tests, and thus, other indicators of formability have been devised that entail less material and testing. A few of these measures are yield strength tension-compression (T-C) asymmetry, strain-rate sensitivity (SRS), and *r*-ratios. The SRS measures the changes in flow stress with changes in strain rate. It is an important indicator of the material resistance to localization during forming operations, and higher values of SRS are more resilient to necking. The *r*-ratio is the ratio between the in-plane strain (or strain rate) and through-thickness strain (or strain rate).[44–47] The strain level at which this ratio is calculated is usually 5 or 10 pct. For Mg and Mg alloys, the *r*-ratio range is broad, from 0 to ~10. The lower the T-C asymmetry ratio, the higher the SRS, and the closer the *r*-ratios are to unity, the more formable the material is considered to be.

In this work, we study the microstructural evolution, including the deformation twinning and underlying effects on the mechanical behavior of Mg-1.3Zn-0.4Ca-0.4Mn alloy, a biocompatible Mg alloy with a dilute concentration of alloying elements. To obtain insight into its formability, we analyze its T-C asymmetry, SRS, and *r*-ratios, when deformed in different sample directions and strain rates, at room temperature. We find that the alloy has a propensity for {1012} twinning under a suitably oriented loading direction. The material exhibits a relatively high SRS (~ 0.015 to 0.025), a saturation *r*-ratio of nearly unity, and a low T-C asymmetry compared to pure Mg and commercial Mg alloys.

II. MATERIAL AND EXPERIMENTAL METHODS

A. *Material*

BIOMG 250 sheets were obtained by thermomechanical processing the as-cast ingot of composition Mg-1.3Zn-0.4Ca-0.4Mn. The final hot rolling pass was a 50 pct reduction to thickness of 2 mm. Afterward, in order to increase the strength, the sheets were subjected to peak aging.

As will be seen shortly, the alloy exhibits a high strength value, despite its low concentration of alloying elements (approximately 2 wt pct) and no RE additions. As will be presented in detail in a subsequent article,[48] the strengthening can be ascribed to grain refinement and the formation of very fine nanometer-scale precipitates such as Guinier–Preston (GP) zones and α-Mn precipitates. These precipitates have been reported in other studies on Mg-Zn-Mn-based alloys.[49–51] The sizes of these α-Mn precipitates in our material range between 3 and 62 nm. Additionally, it was shown that this alloy contains larger precipitates of Ca_2Mg_6Zn type ranging between 170 and 350 nm and Mg_2Ca particles ranging between 165 and 285 nm lying at grain boundaries.

B. *Microstructure*

For microscopy, the samples were ground on abrasive papers #400 to 4000 under running water and then polished on cloths with oil-based diamond suspensions of 3 and 1 μm and then with colloidal silica to obtain a

mirror finish of the surface. After polishing, the samples were cleaned in ethyl alcohol for 3 to 5 minutes in an ultrasonic bath. The microstructure was analyzed using an optical microscope and a Tescan-Lyra scanning electron microscope.

As shown in Figure 1, the present Mg-1.3Zn-0.4Ca-0.4Mn alloy, after rolling and peak aging, has a typical rolling microstructure. The inverse pole figure (IPF) shows that the microstructure has an average grain size of 5 μm. However, the grain structure is bimodal, with a small fraction of grains of size < 5 μm and a large fraction of coarser grains, 5 to 10 μm. As shown in other work,[48] such grain structure results from a high density of pinning precipitates and Zn-Ca solute clusters/segregation at grain boundaries. Solute segregation at the grain boundary not only prevents the preferential growth of the grain boundaries, it also exerts a drag effect on the grain-boundary mobility and pins the boundary. As a result, the extent of grain growth is not high. The grain structure appears relatively homogeneous, with nearly equiaxed grains. This type of microstructure is typical of one that results from dynamic recrystallization after rolling and peak aging. Crystallographic texture measurements indicate that this material has a moderate basal peak on the {0001} pole figure (PF) with a slight spread in the transverse direction (TD). The moderate texture intensity as well as the split in TD is unusual for most rolled Mg alloys.

C. *Mechanical Behavior*

To measure strength, both compression and tension tests are performed along different sample directions. The compression tests were carried out on an Instron model 1350 machine having a load cell capacity of 100 kN equipped with the DAX software and controller at room temperature under 0.001/s strain rate along the rolling direction (RD), TD, and normal direction (ND). The compression tests were carried out to failure. Multiple samples for the same loading direction were tested to ensure repeatability of the results (refer to Appendix A for additional test results). Multiple samples slightly varying in their dimensions considering the sheet thickness were also tested, and again, similar results were obtained. The ND specimens were 2-mm tall with either 2 or 3 mm in-plane square cross sections, while RD and TD samples were either 2- or 3-mm tall with either 2×2, 2×3, or 2×4 mm cross-sectional areas.

For tension testing, the tensile bars were machined per ASTM E8[52–55] as dog-bones having a gage section of 50 mm in length and a 2×12.5 mm cross section. These tests were performed using an MTS biaxial servohydraulic machine with Flextest software and controller. The capacity of the machine is 250 kN, and the tension tests were done in displacement control, with the use of an MTS 623.12E-24 extensometer. These tension tests were performed at room temperature under a range of strain rates, 0.001/s, 0.01/s, and 0.1/s, and along the three in-plane directions, RD, 45 deg, and TD. These tests also went to fracture. As in compression testing, tension tests were repeated to ensure the accuracy and reputability of the data. Consistency in the stress-strain curves per sample category and test conditions was excellent.

We measured the SRS in the three different directions. Such measurements are commonly obtained from (a) a number of uniaxial tensile tests at different strain rates or (b) a single tensile jump test in which each jump corresponds to an increase in the strain rate. Four jumps, each with a doubling of the strain rate, starting with a strain rate of 0.0025, were used. The particular strain rates used in the jump test were 0.0025/s, 0.005/s, 0.01/s, 0.02/s, and 0.04/s, while for tensile tests, strain rates of 0.001/s, 0.01/s, and 0.1/s were used. Based on the data obtained, the SRS of the material can be calculated using $m = \frac{\ln \sigma_2/\sigma_1}{\ln \dot{\varepsilon}_2/\dot{\varepsilon}_1}$, where $\dot{\varepsilon}$ and σ correspond to the particular strain rate and stress.

To measure the instantaneous r-ratios for the RD, TD, and 45 deg samples, uniaxial tension tests were performed at room temperature using the same MTS

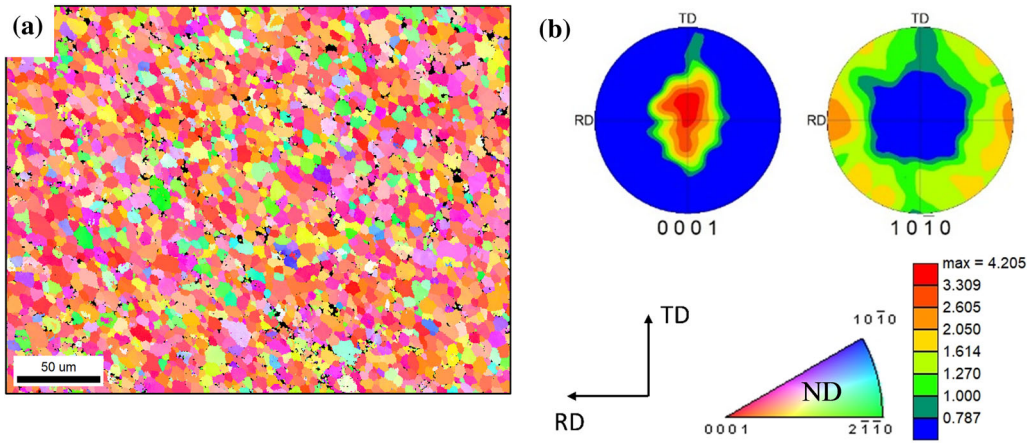

Fig. 1—(*a*) An IPF map showing the grain structure. The frame pertains to the map meaning that the sample direction perpendicular to the map is the ND. The colors in the maps represent the orientation of the ND sample axis with respect to the local crystal lattice frame according to the IPF triangle. (*b*) PFs constructed from EBSD data show the dominance of the {0001} basal plane for peak-aged nanoMAG (Color figure online).

testing machine as used for the tensile testing at a constant, quasi-static strain rate of 0.01/s. Samples were painted with a black and white speckled pattern, and a camera was positioned to record speckle displacement during loading. Using Vic-2D software, a digital image correlation (DIC) was made possible whereby the *in-situ* sample width (normal to the loading direction) and length (parallel to the loading direction) could be measured by observing the displacement of the speckled pattern on the sample surface. The DIC and extensometer strain measurements were cross-validated. The accumulative *r*-ratio of a material describes the ability of that material to resist thinning during tensile or compressive loading. It is defined as $r = \frac{\varepsilon_w}{\varepsilon_t}$, where ε_w and ε_t are the plastic strains along the width and thickness of the sample.[56] Instantaneous *r*-ratio can be calculated for a sample under load using $r_i = \frac{d\varepsilon_w^{pl}}{d\varepsilon_t^{pl}} = \frac{\ln\left(\frac{w_o}{w_i}\right)}{\ln\left(\frac{w_i l_i}{w_o l_o}\right)}$, where the instantaneous strains are calculated from initial and instantaneous sample widths (w_o, w_i) and lengths (l_o, l_i), which are measured using DIC.[56] As mentioned, a value of near unity suggests good formability.

III. RESULTS AND DISCUSSION

A. *Mechanical Behavior*

Figure 2 shows typical stress-strain curves at a quasi-static strain rate of 0.001/s for the Mg-1.3Zn-0.4Ca-0.4Mn alloy. Key quantities, such as the yield strength and ultimate tensile strength (UTS), are summarized in Table I. Comparing the tensile response across the three loading directions, RD, TD, and 45 deg, we observe that the material exhibits plastically anisotropic response. The highest UTS was achieved in the RD and 45 deg direction, with the highest yield strength in the RD. For compression, the strongest response is achieved in the ND. Both compression and tensile responses exhibit inflection points in the hardening rate, which is a typical outcome of underlying twinning deformation; however, the twinning signatures are most pronounced in the compression response. In the RD and TD samples, for which both tension and compression tests could be conducted, we observe a T-C asymmetry, in which the compression response is weaker, in the yield stress and in the flow stress in the early stages of deformation. Overall, the alloy exhibits a good combination of strength and ductility with a UTS in the range of 275 to 310 MPa and up to 25 pct of uniform elongation, which is better than many other biocompatible Mg alloys.[57–59]

As discussed in detail in another work,[48] the material contains a variety of precipitates. It can be expected that these precipitates influence deformation mechanisms of slip and twinning. For instance, basal GP zones can harden the prismatic and pyramidal planes, while the α-Mn precipitates, on the other hand, are spherical and can harden all plane types. Furthermore, since precipitates contain Zn, the Mg matrix is relatively free of Zn, which could increase lattice resistance to dislocation glide compared to the one containing Zn. Atomistic simulations have shown that the addition of Zn in Mg lowers the Peierls barrier and broadens the equilibrium core size of basal dislocations.[60]

B. *r-Ratio*

To calculate the instantaneous *r*-ratios, tensile testing was performed along with DIC. Figure 2(c) presents the instantaneous *r*-ratio as a function of global true strain for each sample orientation. *R*-ratio increases most rapidly in the RD sample, followed by the 45 deg test, and finally the TD test. Remarkably, the *r*-ratios in the RD and 45 deg cases achieve 1 to 1.1, whereas those in the TD reach a maximum of approximately 0.85. Formability is often associated with the lack of twinning. Consistent with this notion, these stress-strain responses from the tensile tests do not exhibit the signs of deformation twinning, which are inflection points and rapid hardening. EBSD of deformed samples will confirm the slip-dominated response in these three cases. For most of the response, the hardening rate decreases with strain. Formability is known to be sensitive to alloying content. The unity and even the near-unity *r*-ratio in the TD direction suggest good formability, which is uncommon in pure Mg and many of its alloys such as AZ31.[61,62] Other Mg alloys that show similar near-unity instantaneous *r*-ratios for all RD, TD, and 45 deg sample orientations when tested in uniaxial tension at a constant strain rate of 10^{-2} s^{-1} are ZE10 and ZEK100 Mg alloys.[61]

C. *Strain-Rate Sensitivity*

Figure 3(b) shows the SRS estimates taken from the strain-rate jump test, and the resulting values are summarized in Tables II and III. We observe a slight anisotropy in the SRS value, being the largest for the RD. Notably, the SRS does not vary substantially with loading direction, likely because the underlying deformation modes are similar. Average values of SRS are positive and estimated to be 0.025 for RD, 0.02 for 45 deg, and 0.015 for TD. Thus, we find that the SRS values and anisotropy are similar to those of fine-grained, pure Mg, which may be expected since this alloy has little solute content and similar grain size. In rolled pure Mg, the SRS values were found to vary from 0.008 in the ND to 0.03 in the in-plane directions.[63] It is worth noting that compared to more concentrated alloys, such as the commercially available and widely used AZ31 Mg alloy (< 0.01), they are relatively higher.[64] Furthermore, in AZ31, the SRS can change drastically from a negative to positive value with loading direction.[65,66]

D. *Deformation Twinning*

In Mg, at room temperature, basal slip is the most easily activated, and then, at higher strain levels, prismatic and pyramidal slip activate. Besides slip, deformation twinning is an important strain accommodation mechanism. Unlike slip, twinning is

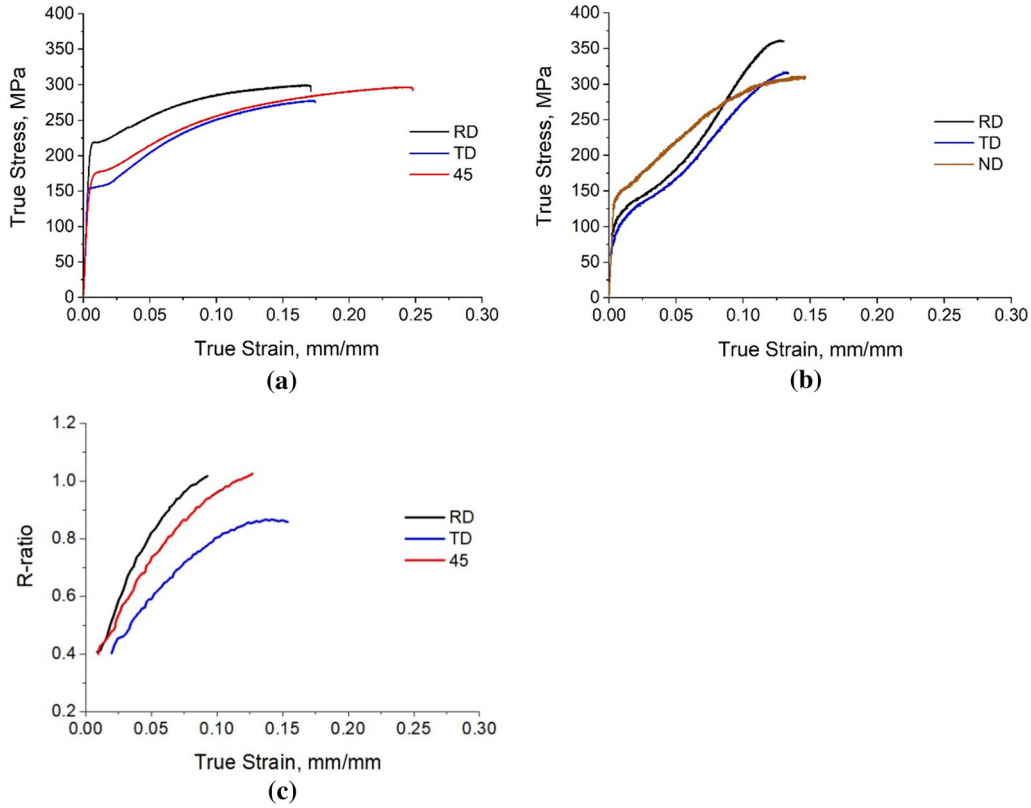

Fig. 2—(*a*) Comparison of true stress–true strain response in tension under 0.001/s strain rate along the three in-plane directions indicated in the legend. (*b*) Comparison of true stress-true strain response in compression under 0.001/s strain rate along the three directions indicated in the legend. (*c*) Instantaneous *r* ratio measured during tension under 0.01/s strain rate along the three in-plane directions.

Table I. Mechanical Properties of the Mg-1.3Zn-0.4Ca-0.4Mn Alloy

	UTS (MPa)	0.2 Pct Offset Yield Strength (MPa)	Uniform Strain (Pct)	True Strain at Fracture (Pct)
RD tension 0.001 s^{-1}	300	219	16.6	17.1
RD tension 0.1 s^{-1}	309	236	10.9	11.9
TD tension 0.001 s^{-1}	278	154	17.3	17.4
TD tension 0.1 s^{-1}	290	154	15.6	16.2
45 deg tension 0.001 s^{-1}	297	164	23.4	24.8
45 deg tension 0.1 s^{-1}	290	173	13	13.9
RD compression 0.001 s^{-1}	365	99	13.0	13.2
TD compression 0.001 s^{-1}	313	82	13.5	13.5
ND compression 0.001 s^{-1}	311	143	13.8	14.3

unidirectional, activated when the *c*-axis is either contracted or extended. In Mg, the most common twinning modes are extension twinning $\{10\bar{1}2\}\langle 10\bar{1}\bar{1}\rangle$, which reorients the lattice by 86.3 deg, and contraction twinning $\{10\bar{1}1\}\langle 10\bar{1}2\rangle$, with reorientation by 56 deg.[67] In addition, double and ternary twinning within these twin types are likely.[68–70] The activation of these slip and twin modes as well as their relative activity is largely dependent on material and microstructural properties, such as initial texture,[28] grain size, and the composition of alloying components, but also on experimental conditions, such as the rate of deformation and test temperature.[71–74] Nonetheless, the simultaneous activity of slip and twinning, the polar nature of twinning, the many possible twin-slip interactions, and the twin reorientation of subgranular domains mean that the mechanisms of plastic deformation in Mg can be quite complicated.

It is known that some suggestion of the activation of twinning in addition to slip can be reflected in the hardening behavior of the uniaxial stress-strain curve.[75,76] Specifically, a stress-strain response with active twinning is normally associated with lower hardening rates and a characteristic inflection point in

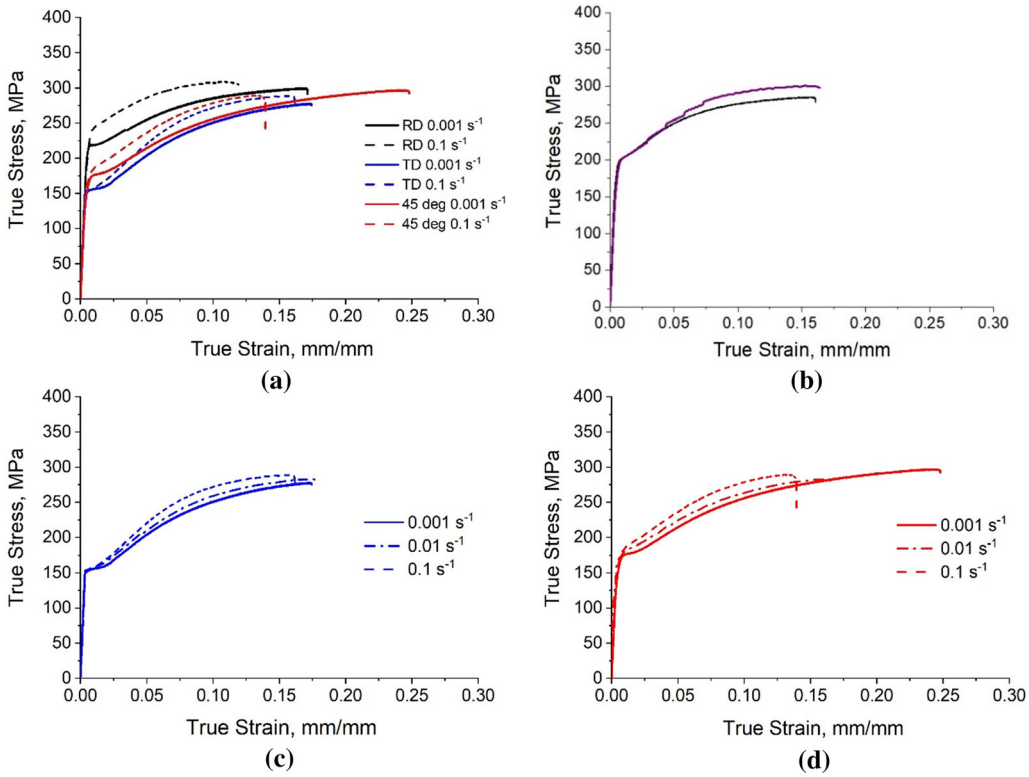

Fig. 3—(*a*) True stress-true strain response under 0.001/s and 0.1/s strain rates for the three in-plane directions. (*b*) Jump test true stress-true strain curve with jumps from 0.0025/s to 0.005/s to 0.01/s to 0.02/s to 0.04/s along with the reference curve for the RD sample. (*c*) True stress-true strain response along the TD as a function of strain rate indicated in the legend. (*d*) True stress-true strain response along the 45 deg relative to the RD as a function of strain rate indicated in the legend.

Table II. SRS Data from the Strain-Rate Jump Test in the RD Tension

	SRS				
Test	Measurement 1	Measurement 2	Measurement 3	Measurement 4	Average *m*
Strain-rate jumps	0.0025 to 0.005	0.005 to 0.01	0.01 to 0.02	0.02 to 0.04	—
m	0.029	0.029	0.024	0.021	0.026

Table III. SRS Data from the Flow Stress Curves for RD, 45 deg, and TD

	SRS				
Test	Measurement 1 at $\varepsilon = 0.02$	Measurement 2 at $\varepsilon = 0.05$	Measurement 3 at $\varepsilon = 0.075$	Measurement 4 at $\varepsilon = 0.1$	Average *m*
RD: 0.001 *vs.* 0.1	0.027	0.026	0.022	0.019	0.024
TD: 0.001 *vs.* 0.1	0.013	0.016	0.017	0.012	0.015
TD: 0.001 *vs* 0.01	0.016	0.013	0.014	0.012	0.014
TD: 0.01 *vs.* 0.1	0.013	0.018	0.019	0.016	0.016
45 deg: 0.001 *vs.* 0.1	0.02	0.022	0.02	0.019	0.02
45 deg: 0.001 *vs.* 0.01	0.02	0.019	0.018	0.016	0.018
45 deg: 0.01 *vs.* 0.1	0.02	0.025	0.022	0.022	0.022

the stress-strain curve, whereas a slip-dominated response is characterized by a uniformly decaying hardening rate with increasing strain. Referring to the mechanical tests shown in Figures 2(a) and (b), the "twinning signature" is clearly evident in compression stress-strain curves in the TD, ND, and RD, while it is

not apparent in the TD and RD tension responses. Furthermore, the TD and RD compression responses have a much lower yield stress, followed by a rapid and positive change in hardening rate, than in their tension responses. Due to deformation twinning, the material exhibits a tension-compression asymmetry in yield stress in the TD and RD, with compression having the weaker response. The analysis of twinning from the stress-strain response alone is qualitative. Twinning may be occurring, albeit in different amounts, in all tested straining directions and strain rates. To quantify twinning further, we employ EBSD analysis on the samples deformed at two different amounts of strain. Figures 4 and 5 show the evolution of microstructure and texture of peak-aged Mg-1.3Zn-0.4Ca-0.4Mn alloy after compression along the RD, the response that suggested a twin-dominated response. It is observed in the EBSD microstructures that after the inflection point in the

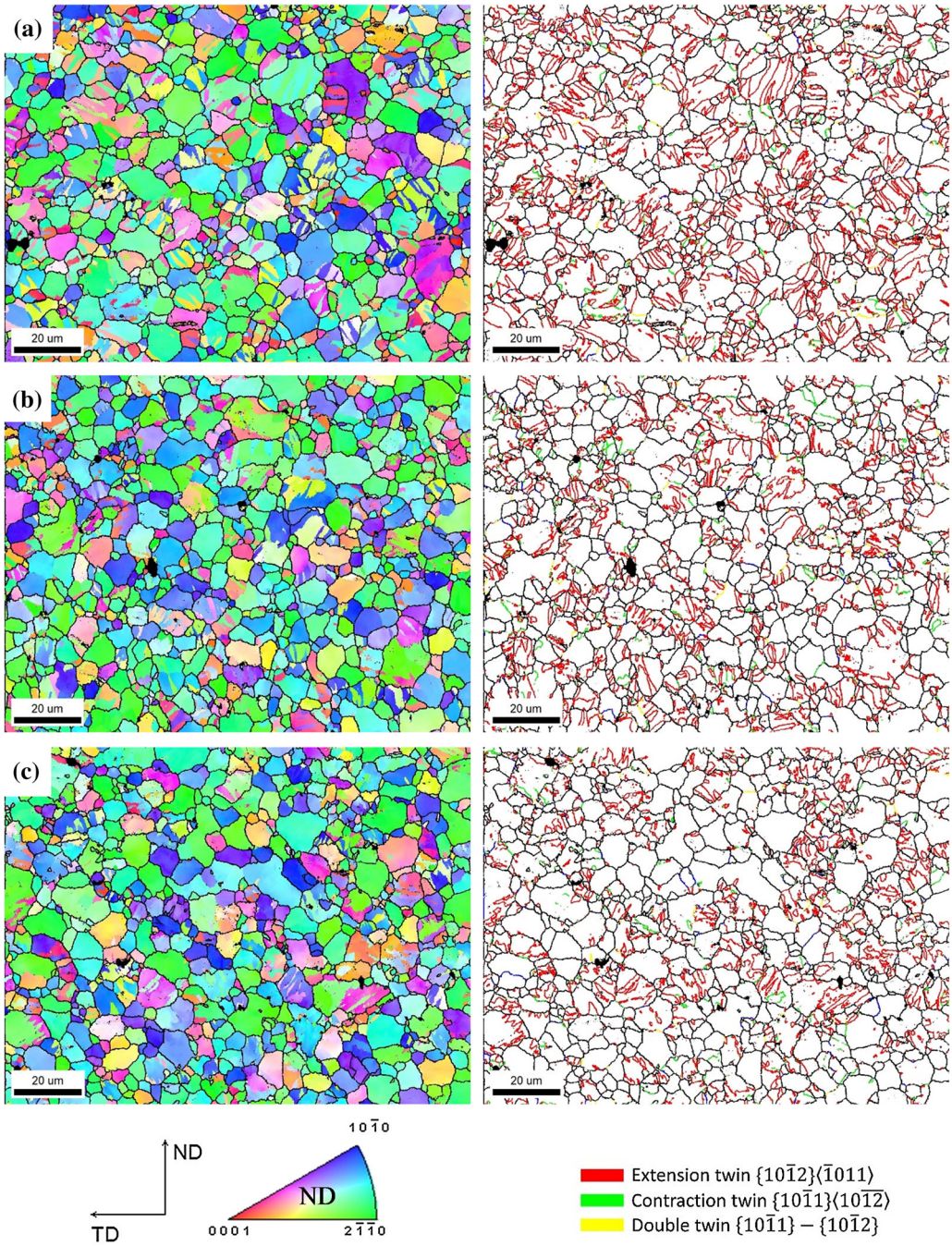

Fig. 4—EBSD maps and blank grain-boundary maps with highlighted twin boundaries showing the evolution of microstructure of the peak-aged Mg-1.3Zn-0.4Ca-0.4Mn alloy after compression along the RD to true strain levels: (*a*) 0.05, (*b*) 0.092, and (*c*) fracture. The estimated twin volume fraction in (a) is 55 pct. The frame pertains to the maps, meaning that the sample direction perpendicular to the maps is the RD. The colors in the maps represent the orientation of the ND sample axis with respect to the local crystal lattice frame according to the IPF triangle (Color figure online).

hardening rate, at approximately 0.05 true plastic strain, profuse twinning is observed with most of the $\{10\bar{1}2\}\langle 10\bar{1}\bar{1}\rangle$ twins. It should be noted that traces of original basal plane peak on $\{0001\}$ PF can also be seen. With further deformation, some grains became entirely reoriented by 86.3 deg. This is also evident from the texture at fracture. Many of the texture components have drastically reoriented from the initial texture, as a consequence of cooperative activity of $\{10\bar{1}2\}\langle 10\bar{1}\bar{1}\rangle$ extension twinning. A similar twin-dominated response is seen in TD compression. Although not shown here, activation of twinning by similar twin types can be expected since the orientation of the texture with respect to the loading direction is similar in TD as in RD.

The questionable test concerns the tension tests in TD and RD, which do not show macroscopic twinning signatures. To check if twinning occurred in one of the tension tests, we elected to analyze the EBSD data after RD tension. As shown in Figure 6, there are no significant changes either in the microstructure or in the texture from the initial state. With nonbasal slip planes and some compression twinning active, the basal planes slightly rotate toward the TD. This analysis suggests that in tension testing of this alloy, the deformation was slip dominated.

The stress-strain responses of this alloy are comparable to those of rolled pure Mg or rolled lightly alloyed Mg material, with a similar initial texture, although as

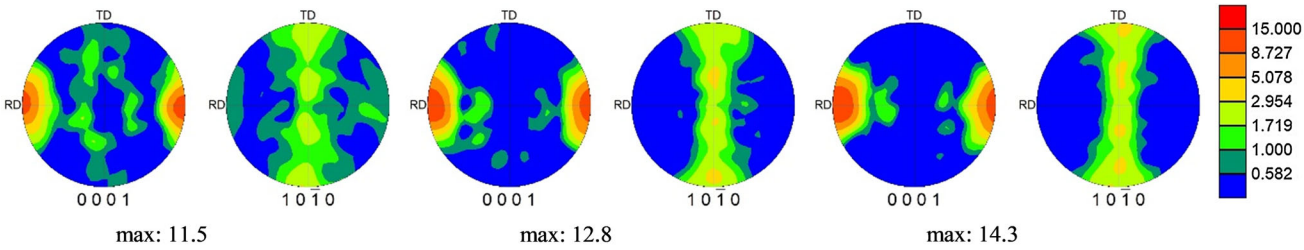

Fig. 5—PFs showing the evolution of texture corresponding to Fig. 4. Every texture is based on multiple EBSD scans of the size like those in Fig. 4 (at least two).

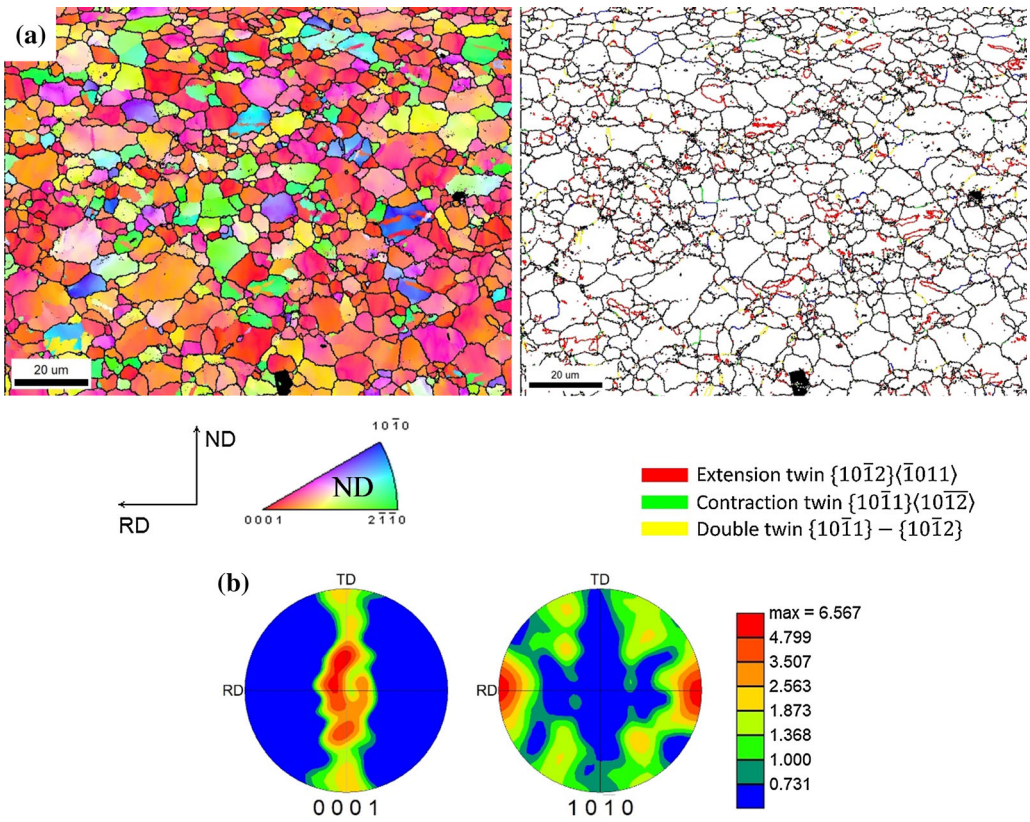

Fig. 6—(*a*) EBSD map along with a blank grain-boundary map highlighting twins and (*b*) PFs showing the texture of peak-aged Mg-1.3Zn-0.4Ca-0.4Mn alloy after tension to fracture along the RD. The frame pertains to the map, meaning that the sample direction perpendicular to the maps is the TD. The colors in the maps represent the orientation of the ND sample axis with respect to the local crystal lattice frame according to the IPF triangle (Color figure online).

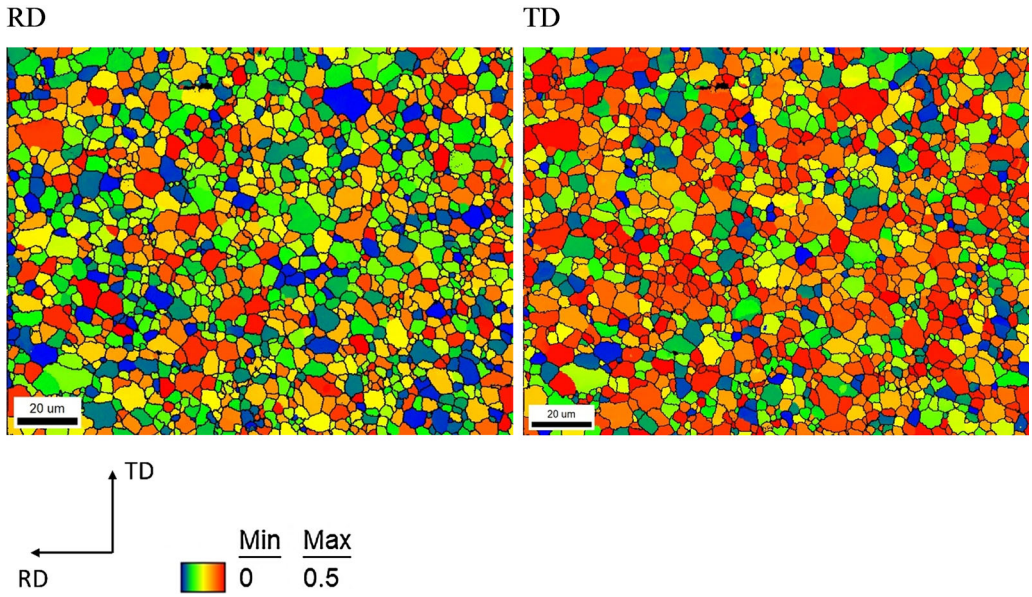

Fig. 7—SF maps for basal slip for the initial peak-aged sheet for tension in the TD and RD. The average value along the RD is 0.24, while that for the TD is 0.3.

mentioned, the one here is substantially weaker twinning.[37–43,71,72] In several prior works, companion polycrystal modeling studies have suggested that the deformation response is governed by basal slip and twinning, with the relative amounts depending on the orientation of the test. For the typical Mg rolling texture, wherein the basal planes are parallel to the rolling plane, applied tension along the RD and TD usually activates a combination of basal slip and some small amounts of contraction twinning, while compression applied along the RD and TD can promote profuse $\{10\bar{1}2\}\langle 10\bar{1}\bar{1}\rangle$ twinning. The deformation twinning in the latter tests contributes significantly to rapid hardening after yield through the barrier effect and texture hardening.[68] In ND compression with the *c*-axis being contracted, deformation is dominated by pyramidal slip.

To gain insight on the differing RD and TD compression cases, we carry out a Schmid factor (SF) analysis for the basal slip contribution based on the initial texture. The SF maps for the RD and TD compression cases are shown in Figure 7. From the analysis, it can be expected that the TD has higher activity of basal slip. This would explain the slight difference in the TD and RD responses. Yield stress in TD tension is slightly lower than that in RD tension. However, the hardening rate in TD tension is slightly higher than that for RD tension because of the greater activity of easy slip and underlying hardening due to slip. In contrast, the hardening rate in TD compression is slightly lower than that for RD compression because of more twinning in RD causing a combination of texture and barrier effect hardening. We can speculate that the higher hardening rate is a result of basal hardening with its profuse activity. The same proposition can be made for the difference in rate sensitivity between the TD and RD responses. Since basal slip is approximately rate insensitive,[77–79] the higher activity of basal slip explains the decreased rate sensitivity in TD compared to RD.

IV. CONCLUSIONS

In this work, the deformation behavior of a novel Mg-1.3Zn-0.4Ca-0.4Mn alloy is studied and discussed. The alloy possesses a moderately strong rolled texture with an average intensity of 4.2 m.r.d. Significantly, the material exhibits high tensile yield and high UTS in all three in-plane directions tested, which is, on average, about 300 MPa, and excellent ductility of up to 25 pct. These values together demonstrate that this alloy performs superior to most of the best biocompatible, dilute alloys to date. Further, the *r*-ratios approaching near unity signify relatively good formability of the alloy. As another advantageous property, the SRS values, which were measured for three in-plane directions, RD, 45 deg, and TD, are shown to be high relative to AZ31, similar to that of fine-grained Mg, and more uniform with respect to direction than coarse-grained pure Mg. These outstanding properties prevailed despite evidence of deformation $\{10\bar{1}2\}\langle 10\bar{1}\bar{1}\rangle$ twinning *via* EBSD, especially for the in-plane compression and some for the in-plane tension.

ACKNOWLEDGMENTS

The authors gratefully acknowledge support from the U.S. National Science Foundation under Grant Nos. CMMI-1727495 (UNH) and CMMI-1728224 (UCSB).

APPENDIX A

In this appendix, we demonstrate in Figure A1 that multiple tests for the stress-strain responses in a fixed rate and loading direction are repeatable.

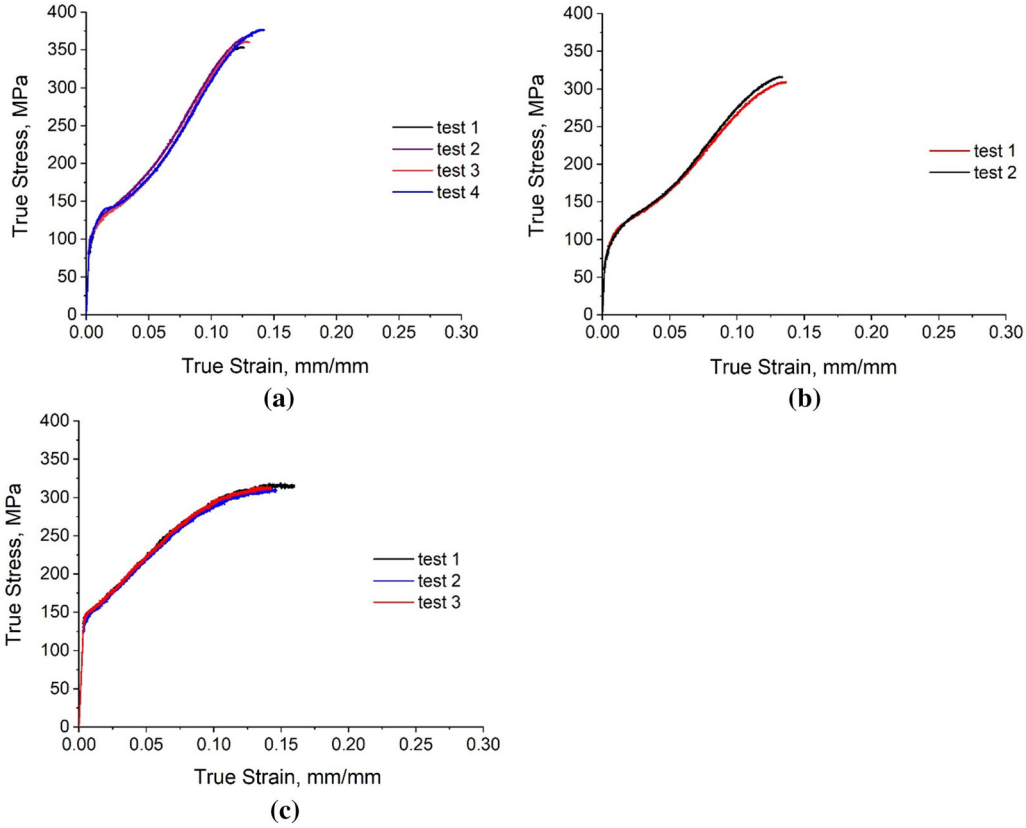

Fig. A1—True stress-true strain curves in compression of the peak-aged Mg-1.3Zn-0.4Ca-0.4Mn alloy along the (*a*) RD, (*b*) TD, and (*c*) ND. Multiple tests per sample category show the repeatibility of the measured results.

REFERENCES

1. M.P. Staiger, A.M. Pietak, J. Huadmai, and G. Dias: *Biomaterials*, 2006, vol. 27, pp. 1728–34.
2. G.L. Song and A. Atrens: *Adv. Eng. Mater.*, 1999, vol. 1, pp. 11–33.
3. F. Witte: *Acta Biomater.*, 2010, vol. 6, pp. 1680–92.
4. H. Hussl, C. Papp, I. Hopfelkreiner, E. Rumpl, and P. Wilflingseder: *Chir. Plast.*, 1981, vol. 6, pp. 117–26.
5. H. Haferkamp, M. Niemeyer, R. Boehm, U. Holzkamp, C. Jaschik, and V. Kaese: *Magnesium Alloys 2000,* 2000, vol. 350 (3), p. 31–41.
6. Y. Shimizu, A. Yamamoto, T. Mukai, Y. Shirai, M. Kano, T. Kudo, H. Kanetaka, and M. Kikuchi: *Interface Oral Health Science*, 2009, vol. 2010, pp. 318–20.
7. E. Zhang and L. Yang: *Mater. Sci. Eng. A*, 2008, vol. 497, pp. 111–18.
8. J. Chen, L. Tan, X. Yu, I.P. Etim, M. Ibrahim, and K. Yang: *J. Mech. Behav. Biomed. Mater.*, 2018, vol. 87, pp. 68–79.
9. C.J. Bettles, M. Gibson, and K. Venkatesan: *Scripta Mater.*, 2004, vol. 51, pp. 193–97.
10. H. Bakhsheshi-Rad, M. Idris, M. Abdul-Kadir, A. Ourdjini, M. Medraj, M. Daroonparvar, and E. Hamzah: *Mater. Des.*, 2014, vol. 53, pp. 283–92.
11. C. Cáceres and A. Blake: *Physica Status Solidi (a)*, 2002, vol. 194, pp. 147–58.
12. D.H. Cho, J.H. Nam, B.W. Lee, K.M. Cho, and I.M. Park: *J. Alloys Compd.*, 2016, vol. 676, pp. 461–68.
13. K. Oh-Ishi, R. Watanabe, C. Mendis, and K. Hono: *Mater. Sci. Eng. A*, 2009, vol. 526, pp. 177–84.
14. F. Rosalbino, S. De Negri, G. Scavino, and A. Saccone: *J. Biomed. Mater. Res., Part A*, 2013, vol. 101, pp. 704–11.
15. N.C. Ferreri, S. Ghorbanpour, S. Bhowmik, R. Lussier, J. Bicknell, B.M. Patterson, and M. Knezevic: *Int. J. Plast*, 2019, vol. 121, pp. 116–33.
16. M. Jahedi, M. Knezevic, and M. Paydar: *J. Mater. Eng. Perform.*, 2015, vol. 24, pp. 1471–82.
17. X. Gao and J.F. Nie: *Scripta Mater.*, 2007, vol. 56, pp. 645–48.
18. B. Zhang, L. Geng, L. Huang, X. Zhang, and C. Dong: *Scripta Mater.*, 2010, vol. 63, pp. 1024–27.
19. T. Homma, J. Hinata, and S. Kamado: *Phil. Mag.*, 2012, vol. 92, pp. 1569–82.
20. J.-F. Nie: *Metall. Mater. Trans. A*, 2012, vol. 43A, pp. 3891–3939.
21. R. Decker, S. LeBeau, D. LaCroix, S. Makiheni, and J. Allison: Springer International Publishing, Cham, 2018, p. 115–23.
22. R. Decker, S. Lebeau, and S. Young: U.S. Patent No. 10,022,470, 2018.
23. B. Zhang, Y. Hou, X. Wang, Y. Wang, and L. Geng: *Mater. Sci. Eng. C*, 2011, vol. 31, pp. 1667–73.

24. R. Ahmad, B. Yin, Z. Wu, and W. Curtin: *Acta Mater*., 2019, vol. 172, pp. 161–84.
25. S. Zhang, X. Zhang, C. Zhao, J. Li, Y. Song, C. Xie, H. Tao, Y. Zhang, Y. He, and Y. Jiang: *Acta Biomater*., 2010, vol. 6, pp. 626–40.
26. H.-X. Li, S.-K. Qin, Y.-Z. Ma, J. Wang, Y.-J. Liu, and J.-S. Zhang: *Int. J. Miner. Metall. Mater*., 2018, vol. 25, pp. 800–09.
27. J. Hofstetter, S. Rüedi, I. Baumgartner, H. Kilian, B. Mingler, E. Povoden-Karadeniz, S. Pogatscher, P.J. Uggowitzer, and J.F. Löffler: *Acta Mater*., 2015, vol. 98, pp. 423–32.
28. S.L. Mannan, S.C. Chetal, Baldev Raj, and S.B. Bhoje: *Selection of Materials for Prototype Fast Breeder Reactor,* Indian Institute of Metals, Calcutta, India, 2003.
29. Y. Ding, C. Wen, P. Hodgson, and Y. Li: *J. Mater. Chem. B*, 2014, vol. 2, pp. 1912–33.
30. P. Jardim, G. Solorzano, and J. Vander Sande: *Mater. Sci. Eng. A*, 2004, vol. 381, pp. 196–205.
31. S.A. Khan, Y. Miyashita, Y. Mutoh, and Z.B. Sajuri: *Mater. Sci. Eng. A*, 2006, vol. 420, pp. 315–21.
32. F. Witte, N. Hort, C. Vogt, S. Cohen, K.U. Kainer, R. Willumeit, and F. Feyerabend: *Curr. Opin. Solid State Mater. Sci*., 2008, vol. 12, pp. 63–72.
33. J. Wang, J. Zhang, X. Zong, C. Xu, Z. You, and K. Nie: *Mater. Sci. Eng. A*, 2015, vol. 648, pp. 37–40.
34. J.A. Helsen and H.J. Breme: *Metals as Biomaterials*, Wiley, Hoboken, NJ, 1998.
35. F. Baruthio, O. Guillard, J. Arnaud, F. Pierre, and R. Zawislak: *Clin. Chem*., 1988, vol. 34, pp. 227–34.
36. M. Aschner, T.R. Guilarte, J.S. Schneider, and W. Zheng: *Toxicol. Appl. Pharmac*., 2007, vol. 221, pp. 131–47.
37. S.R. Agnew: in *Advances in Wrought Magnesium Alloys: Fundamentals of Processing, Properties and Applications,* C. Bettles and M. Barnett, eds., 2012, p. 63–104.
38. M. Lentz, M. Klaus, I.J. Beyerlein, M. Zecevic, W. Reimers, and M. Knezevic: *Acta Mater*., 2015, vol. 86, pp. 254–68.
39. M. Jahedi, B.A. McWilliams, P. Moy, and M. Knezevic: *Acta Mater*., 2017, vol. 131, pp. 221–32.
40. M. Jahedi, B.A. McWilliams, and M. Knezevic: *Mater. Sci. Eng. A*, 2018, vol. 726, pp. 194–207.
41. S. Ghorbanpour, B.A. McWilliams, and M. Knezevic: *Mater. Sci. Eng. A*, 2019, vol. 747, pp. 27–41.
42. S. Ghorbanpour, B.A. McWilliams, and M. Knezevic: *Fatig. Fract. Eng. Mater. Struct*., 2019, vol. 42, pp. 1357–72.
43. D. Nugmanov, M. Knezevic, M. Zecevic, O. Sitdikov, M. Markushev, and I.J. Beyerlein: *Mater. Sci. Eng. A*, 2018, vol. 713, pp. 81–93.
44. W.F. Hosford and R.M. Caddell: *Metal Forming: Mechanics and Metallurgy*, Cambridge University Press, New York, NY, 2011.
45. T.J. Barrett and M. Knezevic: *Comput. Meth. Appl. Mech. Eng*., 2019, vol. 354, pp. 245–70.
46. M. Zecevic and M. Knezevic: *Mech. Mater*., 2019, vol. 136, p. 103065.
47. M. Zecevic, I.J. Beyerlein, and M. Knezevic: *Int. J. Plast*, 2017, vol. 93, pp. 187–211.
48. M.E. Alam, S. Pal, R. Decker, N.C. Ferreri, M. Knezevic, and I.J. Beyerlein: *Sci. Rep*., 2020.
49. L. Tong, M. Zheng, S. Xu, S. Kamado, Y. Du, X. Hu, K. Wu, W. Gan, H. Brokmeier, and G. Wang: *Mater. Sci. Eng. A*, 2011, vol. 528, pp. 3741–47.
50. S.W. Xu, K. Oh-ishi, H. Sunohara, and S. Kamado: *Mater. Sci. Eng. A*, 2012, vol. 558, pp. 356–65.
51. M. Jiang, C. Xu, T. Nakata, H. Yan, R. Chen, and S. Kamado: *J. Alloys Compd*., 2016, vol. 668, pp. 13–21.
52. *Standard Test Methods for Tension Testing of Metallic Materials*, ASTM International, West Conshohocken, PA, 2015.
53. D.H. Smith, J. Bicknell, L. Jorgensen, B.M. Patterson, N.L. Cordes, I. Tsukrov, and M. Knezevic: *Mater. Charact*., 2016, vol. 113, pp. 1–9.
54. S. Gribbin, J. Bicknell, L. Jorgensen, I. Tsukrov, and M. Knezevic: *Int. J. Fatig*., 2016, vol. 93, Part 1, p. 156–67.
55. S. Gribbin, S. Ghorbanpour, N.C. Ferreri, J. Bicknell, I. Tsukrov, and M. Knezevic: *Mater. Charact*., 2019, vol. 149, pp. 184–97.
56. G. Huang, B. Yan, and Z. Xia: *SAE Int. J. Mater. Manufact*., 2011, vol. 4, pp. 385–95.
57. W. Wang, J. Han, X. Yang, M. Li, P. Wan, L. Tan, Y. Zhang, and K. Yang: *Mater. Sci. Eng., B*, 2016, vol. 214, pp. 26–36.
58. S. Agarwal, J. Curtin, B. Duffy, and S. Jaiswal: *Mater. Sci. Eng. C*, 2016, vol. 68, pp. 948–63.
59. M. Lentz, M. Klaus, M. Wagner, C. Fahrenson, I.J. Beyerlein, M. Zecevic, W. Reimers, and M. Knezevic: *Mater. Sci. Eng. A*, 2015, vol. 628, pp. 396–409.
60. Y. Guo, S. Zhang, I.J. Beyerlein, D. Legut, S.-L. Shang, Z. Liu, and R. Zhang: *Acta Mater*., 2019, vol. 181, pp. 423–38.
61. S. Yi, J. Bohlen, F. Heinemann, and D. Letzig: *Acta Mater*., 2010, vol. 58, pp. 592–605.
62. Y. Chino, K. Sassa, A. Kamiya, and M. Mabuchi: *Mater. Sci. Eng. A*, 2006, vol. 441, pp. 349–56.
63. V. Livescu, C.M. Cady, E.K. Cerreta, B.L. Henrie, and G.T. Gray: *Essential Readings in Magnesium Technology*, Springer, New York, NY, 2016, pp. 375–80.
64. R.B. Figueiredo, F.S. Poggiali, C.L. Silva, P.R. Cetlin, and T.G. Langdon: *J. Mater. Sci*., 2016, vol. 51, pp. 3013–24.
65. Y. Chun and C. Davies: *Mater. Sci. Eng. A*, 2011, vol. 528, pp. 5713–22.
66. X. Lin and D. Chen: *J. Mater. Eng. Perform*., 2008, vol. 17, pp. 894–901.
67. M.H. Yoo: *Metall. Trans. A*, 1981, vol. 12A, pp. 409–18.
68. M. Knezevic, A. Levinson, R. Harris, R.K. Mishra, R.D. Doherty, and S.R. Kalidindi: *Acta Mater*., 2010, vol. 58, pp. 6230–42.
69. W.H. Hartt and R.E. Reed-Hill: *Trans. TMS-AIME*, 1967, vol. 239, pp. 1511–17.
70. B.C. Wonsiewicz and W.A. Backofen: *Trans. TMS-AIME,* 1967, vol. 239.
71. M. Ardeljan, I.J. Beyerlein, B.A. McWilliams, and M. Knezevic: *Int. J. Plast*, 2016, vol. 83, pp. 90–109.
72. M. Risse, M. Lentz, C. Fahrenson, W. Reimers, M. Knezevic, and I.J. Beyerlein: *Metall. Mater. Trans. A*, 2017, vol. 48A, pp. 446–58.
73. M. Knezevic, M. Zecevic, I.J. Beyerlein, J.F. Bingert, and R.J. McCabe: *Acta Mater*., 2015, vol. 88, pp. 55–73.
74. M. Knezevic, L. Capolungo, C.N. Tomé, R.A. Lebensohn, D.J. Alexander, B. Mihaila, and R.J. McCabe: *Acta Mater*., 2012, vol. 60, pp. 702–15.
75. M. Knezevic, M.R. Daymond, and I.J. Beyerlein: *Scripta Mater*., 2016, vol. 121, pp. 84–88.
76. T.J. Barrett, R.J. McCabe, D.W. Brown, B. Clausen, S.C. Vogel, and M. Knezevic: *J. Mech. Phys. Solids*, 2020, vol. 138, p. 103924.
77. J.A. García-Grajales, A. Fernández, D. Leary, and A. Jérusalem: *Comput. Mater. Sci*., 2016, vol. 115, pp. 41–50.
78. H. Wang, P. Wu, S. Kurukuri, M.J. Worswick, Y. Peng, D. Tang, and D. Li: *Int. J. Plast*, 2018, vol. 107, pp. 207–22.
79. H. Watanabe and K. Ishikawa: *Mater. Sci. Eng. A*, 2009, vol. 523, pp. 304–11.